ACSNANO
www.acsnano.org
ARTICLE

In Situ Atomic-Scale Probing of the Reduction Dynamics of Two-Dimensional Fe_2O_3 Nanostructures

Wenhui Zhu,[†] Jonathan P. Winterstein,[‡,∥] Wei-Chang David Yang,[‡,§] Lu Yuan,[†] Renu Sharma,*[,‡] and Guangwen Zhou*[,†]

[†]Department of Mechanical Engineering & Materials Science and Engineering Program, State University of New York, Binghamton, New York 13902, United States

[‡]Center for Nanoscale Science and Technology, National Institute of Standards and Technology, Gaithersburg, Maryland 20899, United States

[§]University of Maryland—IREAP, College Park, Maryland 20742, United States

Supporting Information

ABSTRACT: **Atomic-scale structural dynamics and phase transformation pathways were probed, *in situ*, during the hydrogen-induced reduction of Fe_2O_3 nanostructure bicrystals using an environmental transmission electron microscope. Reduction commenced with the α-$Fe_2O_3 \rightarrow \gamma$-$Fe_2O_3$ phase transformation of one part of the bicrystal, resulting in the formation of a two-phase structure of α-Fe_2O_3 and γ-Fe_2O_3. The progression of the phase transformation into the other half of the bicrystalline Fe_2O_3 across the bicrystalline boundary led to the formation of a single-crystal phase of γ-Fe_2O_3 with concomitant oxygen-vacancy ordering on every third {422} plane, followed by transformation into Fe_3O_4. Further reduction resulted in the coexistence of Fe_3O_4, FeO, and Fe *via* the transformation pathway $Fe_3O_4 \rightarrow FeO \rightarrow Fe$. The series of phase transformations was accompanied by the formation of a Swiss-cheese-like structure, induced by the significant volume shrinkage occurring upon reduction. These results elucidated the atomistic mechanism of the reduction of Fe oxides and demonstrated formation of hybrid structures of Fe oxides *via* tuning the phase transformation pathway.**

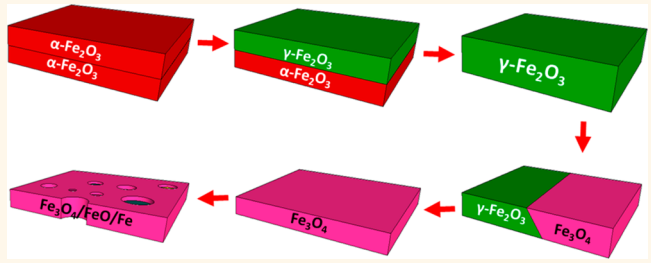

KEYWORDS: *α-Fe$_2$O$_3$, reduction, in situ TEM, phase transformation*

Metal oxides have many important functional properties, ranging from the catalytic activity of partially reduced cobalt oxide to the magnetic data storage capacity of maghemite[1] and the excellent energy capacity of lithium superoxide.[2] These functional properties can be tuned by adjusting stoichiometry, coordination, bonding, and phase of the oxide.[3−5] However, there are significant challenges in controlling these compositional and structural features, particularly at the atomic scale. Controlled reduction of oxides could serve as a viable way to tune the morphology, phase, and atomic structure of oxides and to harness and optimize their functional properties. In order to realize this potential, a fundamental understanding of oxide reduction at the atomic scale is necessary. Unfortunately, this level of understanding is lacking for many oxides because of the difficulty in probing the fast local dynamics of the oxide reduction at the atomic scale using the traditional surface science and bulk materials science techniques. While iron oxides are common compounds that are widespread in nature and can be readily synthesized, understanding the atomistic mechanism of the reduction of iron oxides is even more challenging because of the complicated Fe−O phase diagram.[6]

Nanostructured α-Fe_2O_3 has been studied extensively due to its great potential for a wide range of applications including catalysis,[7−9] water splitting,[10−12] gas sensing,[13,14] and drug delivery.[15,16] Various forms of nanostructured α-Fe_2O_3 have been synthesized,[17−19] such as nanowires,[20−23] nanobelts,[24] nanotubes,[25] nanorods,[26] and nanoblades.[24] There are multiple ways to prepare nanostructured α-Fe_2O_3, such as thermal oxidation,[20,27,28] chemical vapor deposition (CVD),[29,30] and laser ablation.[31] Thermal oxidation of Fe is an efficient and cost-effective method of synthesizing high-quality α-Fe_2O_3 nanostructures at large-scale.[23,27,32−35] Pretreatment of Fe

Received: October 15, 2016
Accepted: December 13, 2016
Published: December 13, 2016

DOI: 10.1021/acsnano.6b06950
ACS Nano 2017, 11, 656−664

foils by sandblasting can be used to form desired morphologies of nanowires or nanoblades.[24,35] In particular, the surface roughness of Fe substrates can be altered to favor the formation of α-Fe_2O_3 nanoblades with a bicrystal structure.[36]

Grain boundaries have been found to influence the mechanical and electronic properties of the crystals.[37] Several types of boundaries such as twin and coincidence-site-lattice boundaries (CSL boundaries or Σ boundaries) are an integral part of bicrystals. Two crystalline grains with a specific combination of misorientation axis and angle result in CSL boundaries. The degree of coincidence is represented by the reciprocal density of common lattice points, denoted as the Σ number.[38] Here we focus on the CSL boundaries with respect to their effect on the reduction behavior of the metal oxides. The α-Fe_2O_3 nanoblades formed from the thermal oxidation of Fe have their two-dimensional (2D) bicrystal boundary parallel to the extended surface. The large grain boundary area associated with the nanoblade morphology makes it an ideal system to study the grain boundary effect on the reduction of metal oxides. As the large surface area is a key factor for catalysis, these α-Fe_2O_3 nanosheets may hold great promise in heterogeneous catalysis either as a catalyst or a catalyst support. We have chosen to study the reduction of these nanosheets in order to probe both the surface stability and the phase transformations that occur in a reducing environment.[39] These conditions are typical of a number of catalytic gas-surface reactions such as methanol oxidation[40,41] and the water–gas-shift reaction[42−44] for which H_2 is involved either as a reactant or a reaction product. By observing the microstructural evolution during reduction processes, especially at the atomic scale, we can establish an in-depth understanding of the material behavior in practical applications and optimize the material properties.

Here, we present our observations of the *in situ* reduction process for the α-Fe_2O_3 nanoblades using an environmental transmission electron microscope (ETEM). Focusing on individual nanoblades, we examined the evolution of morphology and atomic structure of α-Fe_2O_3 nanoblades during reduction. We monitored the reduction process in time-resolved manner by heating α-Fe_2O_3 nanoblades in a H_2 gas flow, interpreted the *in situ* high-resolution TEM (HRTEM) videos frame by frame, and thereby elucidated the atomic processes underlying the morphology and phase evolution of these 2D bicrystal nanostructures.

RESULTS AND DISCUSSION

Figure 1 shows SEM images of the as-prepared α-Fe_2O_3 nanoblades and the samples after H_2-induced reduction to different extents. The morphology of as-prepared nanoblades displays flower-like patterns, with smooth-edged nanoblades perpendicular to the substrate (Figures 1a, b). Typical nanoblade widths range from 1 to 5 μm. The thickness of nanoblades varies from a few nanometers around the edge area to about 20 nm in the center. The as-prepared α-Fe_2O_3 were then reduced by H_2 and examined *ex situ* by SEM. Figure 1c is an SEM image obtained from the sample reduced at 500 °C for 1 h, which shows that the edge area of the nanoblades developed a sawtooth morphology, as indicated in the area marked by a red rectangle in Figure 1c. Figure 1d illustrates the morphology of the nanoblades after the hydrogen-induced reduction at 500 °C for 2 h, showing that the reduced nanoblades developed pits on the large surfaces. Through-holes are also visible around the edge areas of the reduced

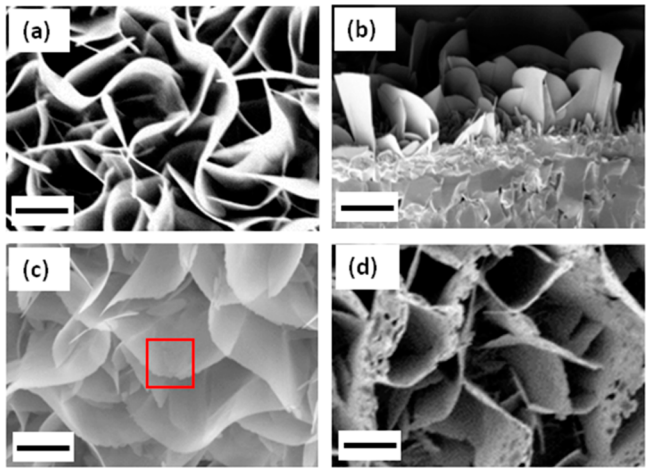

Figure 1. (a) SEM images of α-Fe_2O_3 nanoblades formed by the oxidation of a sandblasted Fe substrate. (b) Cross-section SEM image of the nanoblades. (c) SEM image of nanoblades after 1 h of reduction at 500 °C in H_2, showing the "sawtooth" morphology along the edges (as marked by the red square). (d) SEM image showing the formation of holes after 2 h of reduction. The scale bar is 1 μm.

nanoblades. This is because the edge areas have a smaller thickness and the volume shrinkage induced by the oxide reduction leads to the formation of holes in these thin areas.

A typical low-magnification TEM image of as-prepared Fe_2O_3 nanoblades is shown in Figure 2a. Nanodiffraction (Figure 2b) shows that the nanoblades have a bicrystal structure with the CSL twist boundary (Σ boundary), which agrees with our previous work.[36] The size of area probed to generate the electron diffraction pattern is about 50 nm. The nanodiffraction pattern was taken on the area marked by the red square in Figure 2a. Based on the statistical measurements of multiple nanoblades, 60% of the Fe_2O_3 nanoblades were found to have the CSL twist boundary with a rotation angle 21.8 ± 0.1° between two α-Fe_2O_3 single-crystal platelets in ⟨0001⟩ directions and Σ = 7.[36] Figure 2c is the crystal model based on the diffraction pattern shown in Figure 2b, with two α-Fe_2O_3 unit cells stacked on top of each other and rotated by 21.79° such that the grain boundary is perpendicular to the direction of the incident electron beam. Usually the nanoblades are thicker in the center and thinner along the edge, Figure 2d is a HRTEM image near the edge area. The inset in Figure 2d is a simulated HRTEM image using the structure model shown in Figure 2c and the simulation parameters of a specimen thickness of 4 nm (expected thickness at the edge) and a defocus value of −9 nm, which matches well with the experimental one.

Figure 3 shows the low-magnification *in situ* ETEM observations of the morphology evolution of Fe_2O_3 nanoblades during the hydrogen-induced oxide reduction at 500 °C. To avoid possible long electron beam exposure induced oxide reduction, the beam was on only when taking the TEM images. Figure 3a illustrates the morphology of a typical as-prepared nanoblade before reduction. After 90 min, the formation of a Swiss-cheese-like structure, with tiny pits on it, started to develop (the regions showing brighter contrast in Figure 3b). Upon continued reduction, the nanoblades shrank and pits expanded (Figure 3c). After 240 min of reduction, some regions of the nanoblade decomposed into small particles (Figure 3d).

DOI: 10.1021/acsnano.6b06950
ACS Nano 2017, 11, 656−664

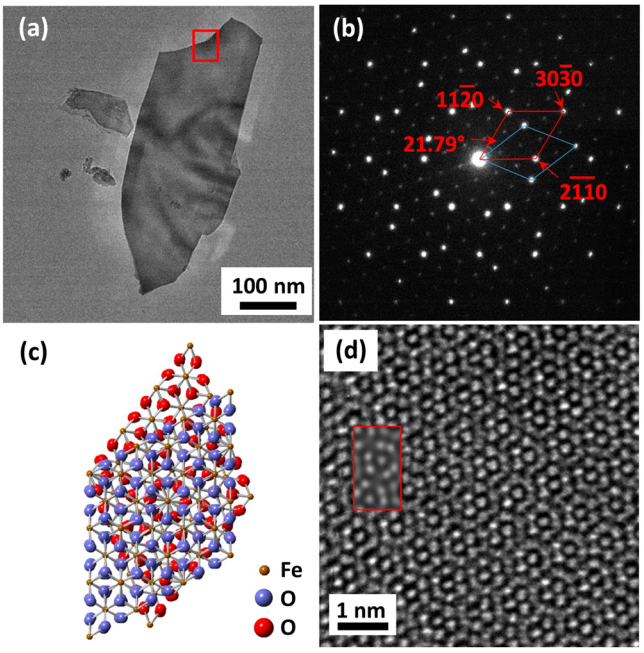

Figure 2. (a) TEM image of a typical as-prepared α-Fe_2O_3 nanoblade (the ghosting effect seen in the image is due to the specimen charging under the electron beam). (b) Nanodiffraction pattern of the bicrystal α-Fe_2O_3 taken at the area marked by the red square shown in (a), which can be indexed as two overlaying α-Fe_2O_3 platelets oriented along the ⟨0001⟩ zone axis, with a CLS twist boundary of 21.79°. (c) An atomic structural model of two overlaying α-Fe_2O_3 unit cells rotated by 21.79° with respect to each other. (d) The HRTEM from the red square area in (a), inset is a simulated HRTEM (outlined by red rectangle) based on the structure model in (c), the image simulation parameters: sample thickness = 4 nm, defocus value = −9 nm.

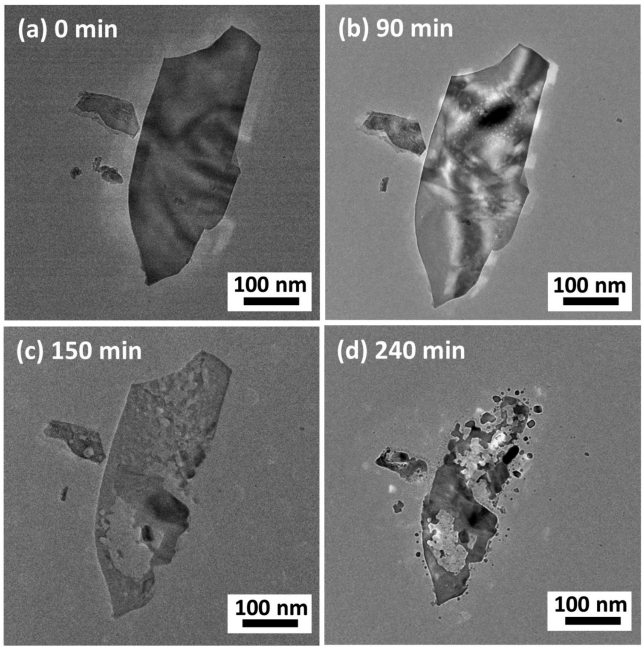

Figure 3. Morphology evolution of α-Fe_2O_3 nanoblade during *in situ* heating at 500 °C with the flow of H_2 gas at the pressure of ≈0.5 Pa. (a) A nanoblade before reduction; (b) the reduction begins with the formation of pits; (c) the nanoblade becomes thinner as the reduction continues; and (d) the nanoblade breaks into small pieces. The observed ghosting effect in the images (a and b) is due to charging of the specimen by the electron beam.

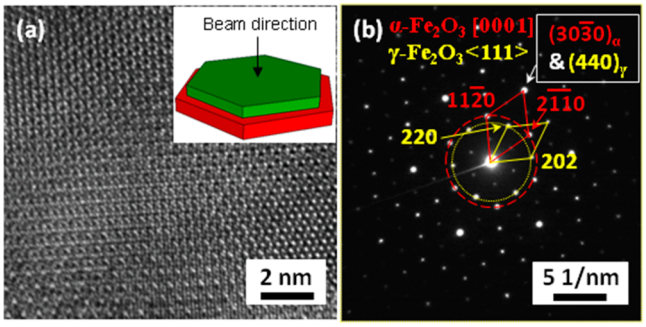

Figure 4. HRTEM image (a) and nanobeam electron diffraction pattern (b) of the nanoblade, showing the parent bicrystal α-Fe_2O_3 nanoblade is transformed into a bilayer structure of α-Fe_2O_3 and γ-Fe_2O_3, with a rotation angle of 30°. The size of area probed to generate the electron diffraction pattern in (b) is about 50 nm, the diffraction pattern was taken from the same region on the nanoblade marked by the red square in Figure 2a.

The reduction process was further characterized at the atomic scale. Figure 4a is an HRTEM image after 30 min of hydrogen-induced reduction at 500 °C. This image was taken from the same region marked by the red square in Figure 2a and obtained by summing up 20 frames after drift-correction to enhance the image contrast. The lattice structure of the reduced sample (Figure 4a) is significantly different from the as-prepared, pure α-Fe_2O_3 sample (Figure 2d), indicating that the oxide underwent a phase transformation. Figure 4a also shows that the lower part of the HRTEM image has a different lattice contrast feature from the upper part, which is caused by the slight deviation of the lower part from the zone axis. This local deviation from the crystallographic orientation is related to the bending effect during the oxide reduction induced phase transformation. Figure 4b is a nanodiffraction pattern obtained from the same area on the nanoblade marked by the red square in Figure 2a. The area probed to generate the electron diffraction pattern was about 50 nm in diameter. The diffraction pattern was taken from the same region in Figure 2a, which consists of two sets of diffraction spots (marked by red and green circles, respectively). One set (marked by red) can be indexed as α-Fe_2O_3 oriented along the [0001] zone axis, and the other (yellow) can be indexed as either γ-Fe_2O_3 or Fe_3O_4 along the ⟨111⟩ zone axis. The latter was confirmed as γ-Fe_2O_3 by measuring the white line ratio of the Fe L edge in electron energy loss spectra (EELS) (Figures 5d, e). The existence of α-Fe_2O_3 diffraction spots indicated that the nanoblade was partly transformed to γ-Fe_2O_3. The phase transformation, expected as the first step of reduction from single-crystal reduction,[32] started from the top layer of the bicrystals because of its direct in contact with the H_2 gas, whereas the bottom part of the nanoblade was still not reduced because of its exposure to H_2 was limited by the SiN_x support membrane of the TEM grid. From the composite diffraction pattern (Figure 4b), an in-plane rotation angle of 30 ± 0.1° was measured between the γ-Fe_2O_3 ⟨111⟩ and α-Fe_2O_3 ⟨0001⟩ patterns. The orientation relationships are α-$Fe_2O_3(0001)//\gamma$-$Fe_2O_3(111)$ and α-Fe_2O_3 $\langle 10\bar{1}0\rangle//\gamma$-$Fe_2O_3$ ⟨110⟩. The $\{30\bar{3}0\}$ planes in α-Fe_2O_3 are aligned with {440} in γ-Fe_2O_3 because the bright diffraction spots of α-Fe_2O_3 $\{30\bar{3}0\}$ overlap with γ-Fe_2O_3 {440} ($g_{\{30\bar{3}0\}}$ = 6.8 nm^{-1}, $g_{\{440\}}$ = 6.9 nm^{-1}). The preferred orientation

DOI: 10.1021/acsnano.6b06950
ACS Nano 2017, 11, 656−664

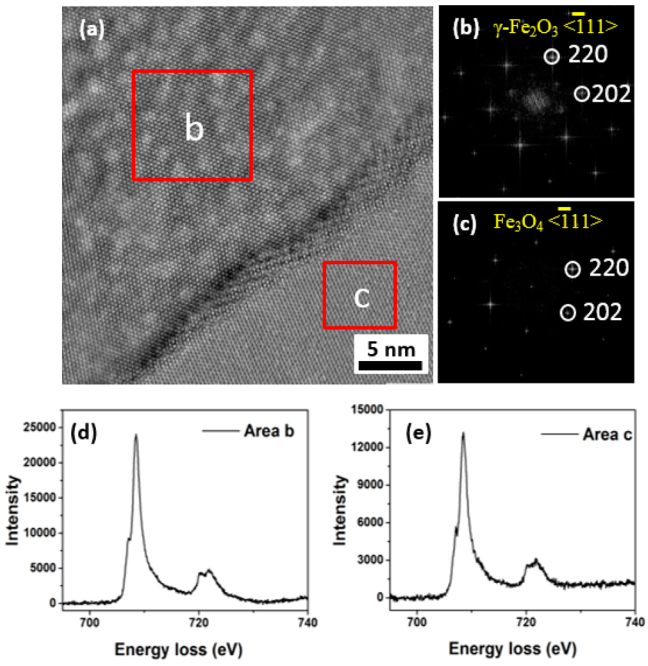

Figure 5. (a) *In situ* HRTEM visualization (supplemental *in situ* TEM video 1) of the transformation from γ-Fe_2O_3 to γ-Fe_2O_3-superstructure in the upper-left corner of the image. (b, c) The diffractograms from red boxed regions b and c, in (a), respectively. Note the presence of extra spots in (b), which are related to the ordering of oxygen vacancies in the γ-Fe_2O_3 region in the upper-left corner. (d, e) EELS spectra from the regions marked by red boxes b and c in (a), respectively. Both regions b and c marked in (a) are γ-Fe_2O_3, but the white line ratio in (e) is 5.05, slightly lower than 5.23 in (d), indicating the γ-Fe_2O_3 in upper-left corner region as marked by red box b in (a) has a slightly lower oxidation state induced by oxygen vacancies (details of the measurements and the analysis are given in the Supporting Information).

relationship induced by the α-$Fe_2O_3 \rightarrow \gamma$-$Fe_2O_3$ transformation can be attributed to the fact that both the α-Fe_2O_3(0001) and γ-Fe_2O_3(111) planes are close-packed planes with an in-plane six-fold symmetry at the interface, which is also in agreement with the previous report on the transformation γ-$Fe_2O_3 \rightarrow \alpha$-$Fe_2O_3$.[45] The 30° rotation between the two platelets with the α-Fe_2O_3/γ-Fe_2O_3 bilayer structure is likely the most stable arrangement of the two structures that involves the minimum rearrangement of atoms in their close-packed planes from the transformation of one platelet of the parent bicrystal α-Fe_2O_3 that has the original 21.79° rotation of the two platelets to the γ-Fe_2O_3.

As the reduction proceeded, the remaining α-Fe_2O_3 platelet (the bottom crystal) continued to transform to γ-Fe_2O_3. Figure 5a is a HRTEM image captured during the *in situ* observation of the oxide reduction induced structure transformation in the area marked with the red square in Figure 2a, which shows two different lattice structures with moiré fringes in their boundary region. Figures 5b, c are diffractograms obtained from the regions marked by red squares b and c in Figure 5a, respectively. By indexing the diffractograms, it can be concluded that both regions b and c have the cubic structure that can be either γ-Fe_2O_3 or Fe_3O_4. At this point, the CSL grain boundary disappears in the diffractograms. The absence of the grain boundary indicates that the other component (α-Fe_2O_3) of the bicrystal nanoblades also transformed into γ-Fe_2O_3 (or Fe_3O_4), and the newly formed structure is perfectly aligned with the already transformed γ-Fe_2O_3 component because the diffractograms of the HRTEM images yield only one set of diffraction spots (either Figure 5b or c). The sequential transformation of the two crystals, stacked on top of each other, indicates that slow diffusion of the reactants (hydrogen and oxygen) or the accumulation of oxygen vacancies at the bicrystal boundary (*i.e.*, the boundary acts as a sink for vacancies) delayed the onset of reduction of the bottom crystal. As mentioned earlier, the space groups and lattice constants of γ-Fe_2O_3 and Fe_3O_4 are very similar (γ-Fe_2O_3: space group $P4_132$, $a = b = c = 0.8347$ nm; Fe_3O_4: space group $Fd\bar{3}m$, $a = b = c = 0.8394$ nm) and cannot be distinguished on the basis of the diffractograms. In Figure 5b, there are two extra superlattice spots, indicating the d spacing of the newly ordered planes is 3 times of that of the original γ-Fe_2O_3 {422} crystal planes. This is most probably due to the ordering of oxygen vacancies parallel to {422} planes, with the d spacing three times of that of {422}, *i.e.*, with a vacancy present on every third {422} plane. The ordering of oxygen vacancies parallel to {422} planes was also confirmed using HRTEM image simulation. The observed ordering is just one of the metastable vacancy ordered phases, as other vacancy ordered phases such as with ordering of oxygen vacancies on every fourth $(1\bar{1}2)$[46] or every 10th $(30\bar{3}0)$[32] planes were also reported.

Figures 5d, e are the respective EELS spectra of regions b and c marked by the red squares in Figure 5a after background removal and deconvolution. Since γ-Fe_2O_3 and Fe_3O_4 are both cubic structures with very similar lattice constants, it is impossible to distinguish them by electron diffraction. However, the oxidation state of Fe is different in the two structures. Therefore, the L_3/L_2 ratio, which is proportional to the oxidation state, can be used to identify them. The L_3/L_2 ratios were calculated and compared with standard samples (commercial α-Fe_2O_3, γ-Fe_2O_3, Fe_3O_4, and FeO) to distinguish between the γ-Fe_2O_3 and Fe_3O_4 phases (details of the measurements and the analysis are given in the Supporting Information). Combined measurements from the diffractogram and EELS confirmed that region b in Figure 5a has the γ-Fe_2O_3 structure with the ordering of oxygen vacancies and region c is Fe_3O_4. The γ-Fe_2O_3 with the oxygen-vacancy ordering is an intermediate structure formed during the reduction process.[46] This is because of the continuous supply of H_2 during the *in situ* reduction, for which O atoms continuously departed from the oxide by reacting with adsorbed H to form H_2O molecules that desorbed from the oxide surface. Therefore, oxygen vacancies were continuously generated in the oxide and can dynamically self-order into a sequence of superstructures[46] as the reduction proceeded. The superstructure observed from our experiments might be one of the relatively more stable oxygen-vacancy ordered superstructures.

With the continuous accumulation of oxygen vacancies, the intermediate phase of γ-Fe_2O_3 became increasingly unstable and transformed into the more stable Fe_3O_4. It can be noted from Figure 5a that there are many tiny pits or internal voids (brighter dots) formed in region b. They are clusters formed by the coalescence of excess oxygen vacancies. It is also interesting to note from Figure 5a that there are no pits in the Fe_3O_4 region (*i.e.*, the lower-right corner), suggesting that the Fe_3O_4 region is relatively free of oxygen vacancies and the reduction occurred mainly in the γ-Fe_2O_3 region at this stage. This is reasonable because the lower-right region already underwent the γ-$Fe_2O_3 \rightarrow Fe_3O_4$ transformation, in which oxygen

DOI: 10.1021/acsnano.6b06950
ACS Nano 2017, 11, 656–664

vacancies were annihilated. As shown in Figure 5a, the Moiré fringe contrast occurred in the γ-Fe_2O_3/Fe_3O_4 interface region because the interface was inclined with respect to the incident electron beam. The occurrence of the Moiré fringe contrast only in γ-Fe_2O_3/Fe_3O_4 interface region demonstrated clearly that lower-left corner region was completely transformed to Fe_3O_4 in the through-thickness direction of the nanoblade and the γ-Fe_2O_3 → Fe_3O_4 transformation propagated laterally toward the γ-Fe_2O_3 region. This manner of the phase transformation is very different from the first stage of reduction of the parent α-Fe_2O_3 bicrystals, for which only one of the two platelets of the bicrystal was first transformed into the γ-Fe_2O_3, resulting in the γ-Fe_2O_3/α-Fe_2O_3 bilayer structure.

Figure 6 illustrates a sequence of *in situ* TEM images (extracted from supplemental *in situ* HRTEM video 2) showing the next reduction step after the γ-Fe_2O_3 → Fe_3O_4 transformation was completed. The diffractograms of the two regions marked by the red squares in Figure 6c show that the newly transformed region (the slightly darker gray region) is

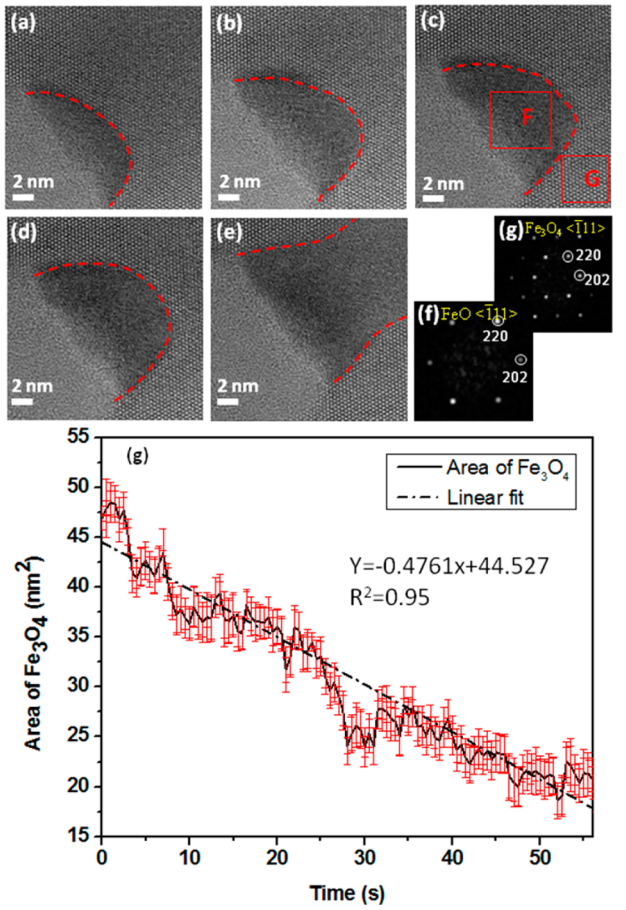

Figure 6. Time sequence of high-resolution TEM images (extracted from supplemental *in situ* TEM videos 2 and 3) showing the phase transformation from Fe_3O_4 to FeO: (a) 0.5 s, (b) 25 s, (c) 50 s, (d) 60 s, (e) 75 s. (f, g) The diffractograms of the regions marked by "F" and "G" in (c), showing that the region before transformation (region "G") is Fe_3O_4 ⟨111⟩ and then transform to FeO ⟨111⟩ (region "F") with the orientation relationship of the topotactic transformation of Fe_3O_4 ⟨111⟩//FeO ⟨111⟩. (g) The reduction rate of the oxide measured from the *in situ* TEM video of the shrinkage of the Fe_3O_4 region. The error bars give single standard deviation uncertainties based on multiple measurements.

FeO, while the rest is Fe_3O_4. The propagation of the FeO region was accompanied by the concurrent retraction of the Fe_3O_4 region, which clearly demonstrated the transformation path Fe_3O_4 → FeO. The *in situ* TEM images shown in Figures 6a–f also confirm that the reduction reaction was a topotactic transformation with the crystallographic orientation relationship of Fe_3O_4 ⟨111⟩//FeO ⟨111⟩. This orientation relationship is preferred because both Fe_3O_4 and FeO are cubic (Fe_3O_4: space group $Fd\bar{3}m$, a = 0.8394 nm; FeO: space group: $Fm\bar{3}m$, a = 0.4354 nm), and the Fe_3O_4 → FeO transformation along the Fe_3O_4(111)/FeO(111) interface would require minimal atomic rearrangement because the (111) planes are the closest-packed planes for both structures.

The reduction kinetics of the Fe_3O_4 component shown in Figure 6 was also determined by measuring the shrinkage of the Fe_3O_4 from the *in situ* TEM video. To calculate the reaction rate, an automated image processing scheme (AIPS), which is a combination of algorithms developed at NIST and publically available, was used to obtain structural information from each frame extracted from videos. The video of atomic positions corresponding to the HRTEM video is available in the Supporting Information (video 3). After identifying the atomic positions and measuring the spacing between every two nearest neighbors, the area occupied by Fe_3O_4 structure in each frame can be assigned and calculated. The Fe_3O_4 area (Figure 6g) was measured as a function of time to determine the reaction rate. The reduction kinetics can be fitted linearly, and the reaction rate (slope) was determined to be 0.48 ± 0.3 $nm^2 \cdot s^{-1}$, where the uncertainty is a single standard deviation as determined by the fitting procedure. A linear fit assumed a zero-order reaction or a pseudozero-order reaction, which was reasonable in this case because only a small fraction of the Fe_3O_4 reacts, and this fraction was continuously replenished from the larger pool (the parent nanowire). Fitting the data in Figure 6g with an exponential decay function expected for a higher-order reaction gave R^2 = 0.95, which was an equivalent confidence level to the linear fit. The uncertainty shown in Figure 6g was given by the standard deviation of multiple measurements. Because of the similarity of R^2 for the exponential *vs* linear fits, it is not sufficient to determine the order of reaction for this transformation that would require the measurements on the reaction rate over many reactant concentrations.

The reduction of metal oxides has been traditionally described using an interface-controlled model, *i.e.*, the reduction rate depends on the interface area between the reduced phase and the parent oxide.[47−50] As shown in Figures 6a–f, the Fe_3O_4/FeO interface area became larger during the course of the reduction, implying that the reaction rate should increase with time if the reduction was controlled by the Fe_3O_4/FeO interface. The linear time dependence of the transformation from Fe_3O_4 to FeO observed in our experiment suggested that the reduction was a surface reaction limited process, which can be either due to the surface adsorption of H_2 molecules or the removal of H_2O molecules.

The reduced nanoblades show a porous morphology with sawtooth-like edges after 120 min of heating in the H_2 gas flow (Figure 7a). The clustering of vacancies resulted in the formation of craters, while the nanoblade body still remained as Fe_3O_4 (Figures 7a, b and inset diffractograms). The diffractogram from the area marked in Figure 7c indicates the existence of an amorphous structure, which is the SiN_x supporting membrane of the TEM grid, confirming the pit formation and the development of a through hole in the pit

DOI: 10.1021/acsnano.6b06950
ACS Nano 2017, 11, 656–664

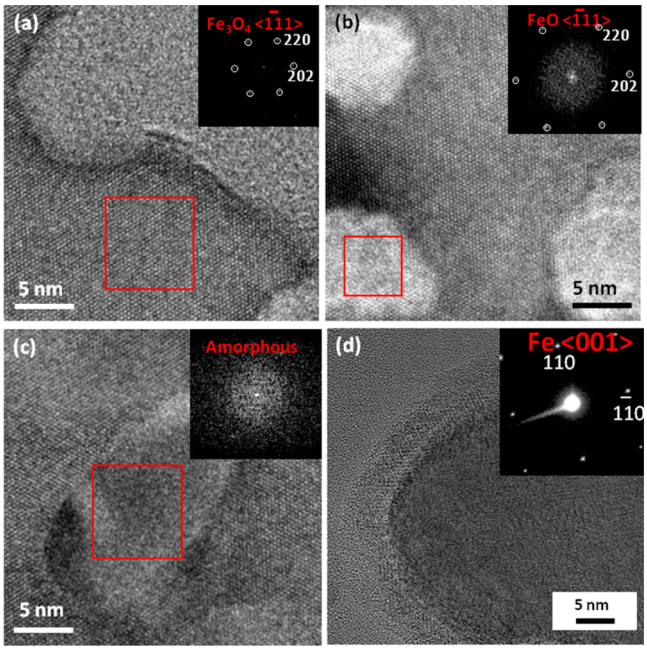

Figure 7. (a) HRTEM of the nanoblade edge region after heating in H_2 for 61 min, showing the sawtooth structure formed along the edge; the diffractogram of the marked square area is Fe_3O_4 ⟨111⟩. (b) HRTEM image showing the formation of pits; the diffractogram of the pit area is consistent with FeO ⟨111⟩. (c) HRTEM image with the formation of porous structure on the nanoblade; the diffractogram of the marked area indicates the presence of an amorphous material, which is the SiN_x membrane of the TEM grid, confirming the formation of a through hole. (d) HRTEM image obtained from a Fe nanoparticle formed during the final stage of the reduction; the inset is a nanobeam diffraction pattern along the Fe ⟨001⟩.

area. The morphology was in accordance with the SEM observation shown in Figure 1d and the *in situ* TEM observation in Figure 3d. At this point, the structure of the nanoblade consists of two oxides of iron (Fe_3O_4 and FeO) and metallic Fe. Eventually, the entire α-Fe_2O_3 nanoblade was transformed into metallic Fe and fell apart into multiple Fe nanoparticles (Figure 7d and the inset diffraction pattern) due to the considerable specific volume shrinkage from α-Fe_2O_3 (cell volume = 0.5816 nm^3) to Fe (cell volume = 0.0439 nm^3). As shown in Figure 7d, the Fe nanoparticle has a core–shell structure with a thin layer of ultrafine nanocrystals grown on the surface. This is because metallic Fe nanoparticles are highly reactive[51] and can easily reoxidize immediately to form a thin surface oxide layer even in the low partial pressure of oxygen present in the TEM column. The *in situ* TEM observations demonstrated that the reduction by H_2 results in the formation of a porous structure in the parent Fe_2O_3 nanoblade, followed by its disintegration into Fe nanoparticles. Such dramatic morphology changes are induced by the significant volume shrinkage that occurs during the H_2-induced reduction-driven phase transformation from α-Fe_2O_3 to metallic Fe upon the loss of lattice oxygen from the oxide.

The reduction for bulk α-Fe_2O_3 by H_2 follows the reaction sequence of α-Fe_2O_3 → Fe_3O_4 → FeO → Fe[52] or α-Fe_2O_3 → Fe_3O_4 → Fe.[53] By contrast, we find the reduction of α-Fe_2O_3 nanoblades follows the transformation sequence of α-Fe_2O_3 → γ-Fe_2O_3 superlattice (Figure 4) → Fe_3O_4 (Figure 5) → FeO (Figure 6) → Fe (Figure 7). The absence of the polymorph transition of α-Fe_2O_3 → γ-Fe_2O_3 in the reduction of the bulk oxide can be related to the kinetic constraints associated with the substantial distortion in the cell parameters of the α-Fe_2O_3 (hexagonal, $a = b = 0.5036$ nm, $c = 1.3749$ nm) to obtain γ-Fe_2O_3 (cubic, $a = b = c = 0.8347$ nm). However, such a kinetic hindrance to the γ-Fe_2O_3 formation may vanish for the reduction of α-Fe_2O_3 nanoblades because a large fraction of the atoms are located in a close proximity to the surface, which facilitate oxygen removal and self-ordering of oxygen vacancies as well as the cell distortion. Therefore, the reduction of the 2D nanosheets proceeds with more substeps compared with their bulk counterpart.

Figure 8 schematically summarizes the reduction pathway of the bicrystal α-Fe_2O_3 with the bicrystal boundary observed

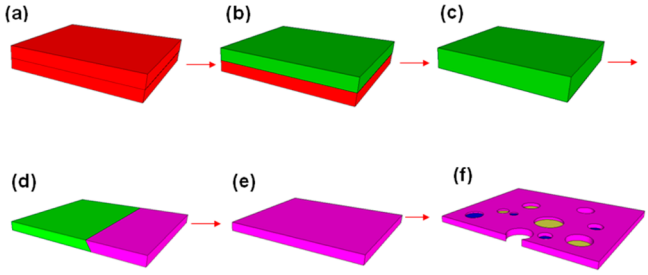

Figure 8. Schematic illustration of the reduction pathway of α-Fe_2O_3: (a) bicrystal α-Fe_2O_3, (b) α-Fe_2O_3/γ-Fe_2O_3 bilayer structure, (c) single-crystal γ-Fe_2O_3 superlattice, (d) γ-Fe_2O_3 → Fe_3O_4, (e) Fe_3O_4, (f) a Swiss-cheese-like structure consisting of Fe_3O_4, FeO, and Fe nanoparticles. Red: α-Fe_2O_3; green: γ-Fe_2O_3; purple: Fe_3O_4; blue: FeO; yellow: Fe.

from our *in situ* TEM experiments, where the reduction reaction starts from the surface that is directly exposed to H_2. The α-Fe_2O_3 nanoblades are first transformed into an α-Fe_2O_3/γ-Fe_2O_3 bilayer structure as one of the α-Fe_2O_3 platelets transforms into γ-Fe_2O_3. The α-Fe_2O_3/γ-Fe_2O_3 hybrid then transforms to a single-crystal γ-Fe_2O_3 nanoblade by converting the other α-Fe_2O_3 platelet into γ-Fe_2O_3. With continued H_2 exposure, oxygen vacancies form in the γ-Fe_2O_3 nanoblade and self-order into a superstructure. However, if both surfaces are directly exposed to H_2, γ-Fe_2O_3 formation can occur on the two surfaces of the nanoblade with their respective crystallographic orientation with the parent α-Fe_2O_3 grain. As a result, a bicrystal γ-Fe_2O_3 nanosheet may develop, instead of forming the α-Fe_2O_3/γ-Fe_2O_3 bilayer structure and then a single-crystal γ-Fe_2O_3 sheet as shown schematically in Figures 8(b and c). The continued accumulation of oxygen vacancies in γ-Fe_2O_3 results in the formation of clusters of oxygen vacancies with the concomitant γ-Fe_2O_3 → Fe_3O_4 transformation. The subsequently formed Fe_3O_4 transforms into FeO and then to Fe upon further H_2 exposure at the elevated temperature. Due to the significant volume shrinkage along the transformation pathway of α-Fe_2O_3 → γ-Fe_2O_3 → Fe_3O_4 → FeO → Fe, the parent α-Fe_2O_3 nanoblades disintegrate into Fe nanoparticles.

CONCLUSIONS

In summary, we have monitored the H_2-induced reduction process of α-Fe_2O_3 nanoblades and elucidated the reduction mechanism at the atomic scale. The parent α-Fe_2O_3 nanoblades have the CSL boundary formed by two platelets with a rotation angle of 21.79°. The reduction of the bicrystal α-Fe_2O_3 nanoblades commences with the transformation of one of the

DOI: 10.1021/acsnano.6b06950
ACS Nano 2017, 11, 656–664

platelets to γ-Fe_2O_3, resulting in a nanoblade of the α-Fe_2O_3/γ-Fe_2O_3 hybrid structure formed by the alignment of the α-Fe_2O_3 and γ-Fe_2O_3 platelets with a rotation angle of 30°. The α-Fe_2O_3 platelet in the α-Fe_2O_3/γ-Fe_2O_3 bilayer structure transformed into γ-Fe_2O_3, thereby forming a 2D single-crystal γ-Fe_2O_3. Upon further loss of lattice oxygen, the γ-Fe_2O_3 developed into a γ-Fe_2O_3 superstructure with the ordering of oxygen vacancies followed by the nucleation and growth of Fe_3O_4. Upon continued reduction, the ordered oxygen vacancies aggregated to form pits in the γ-Fe_2O_3 matrix. The transformed Fe_3O_4 was further reduced into FeO. Finally, the nanoblades were reduced to metallic iron and disintegrated into multiple Fe nanoparticles. These observations demonstrate that a high degree of control over the morphology, crystal structure, and oxidation state of the oxide nanostructures can be made by controlled oxide reduction.

METHODS

Materials Preparation. The α-Fe_2O_3 samples used for the *in situ* reduction experiments were prepared by the thermal oxidation of polycrystalline Fe foils (99.99% pure). The high-purity Fe foils were first sandblasted using glass-bead abrasives with diameters ranging from 150 to 250 μm for 60 s at a pressure of 689.5 kPa (100 pounds per square inch) to modify the surface roughness. The sandblasted Fe foils were then thoroughly rinsed in deionized water followed by ultrasonication in acetone for 5 min. The cleaned iron foils were then placed on a substrate heater in a vacuum chamber, and the sample temperature was monitored by a K-type thermocouple in contact with the substrate heater. The chamber was pumped to vacuum ($\approx 3 \times 10^{-4}$ Pa) and then filled with oxygen gas at a pressure of ≈270 Pa (99.999% pure) and sealed. The Fe foil was then heated to 600 °C at a rate of ≈20 °C min^{-1} in the oxygen gas and oxidized at 600 °C for 60 min. This yielded well-aligned, crystalline α-Fe_2O_3 nanoblades perpendicular to the Fe substrate. More details about the formation of nanostructured Fe_2O_3 by the thermal oxidation of Fe can be found in our previous work.[20,24,45,54] *Ex situ* reduction of the as-prepared α-Fe_2O_3 nanoblades was conducted in the same vacuum chamber by switching to the H_2 gas flow and at the reduction temperature ranging from 500 to 600 °C. The morphology changes before and after the reduction were examined by field-emission scanning electron microscopy (FEG-SEM).

***In situ* TEM Characterization.** *In situ* experiments to monitor oxide reduction were performed in a dedicated ETEM equipped with an objective-lens aberration corrector and a gas manifold that enables control of the flow rate and partial pressure of various gases in the specimen area.[55] As-prepared α-Fe_2O_3 nanoblades were scratched off the Fe substrate and were dispersed in isopropanol by ultrasonication, followed by drop casting the suspension onto SiN_x membrane TEM grids. These were then loaded onto a heating holder and inserted in the ETEM. In our experiments, hydrogen (99.999% pure) was first flowed through a liquid nitrogen trap to condense water molecules and was then introduced into the specimen area in the ETEM column at a partial pressure of 0.5 Pa. The sample was then heated to 500 °C in the H_2 flow. *In situ* TEM observations, acquisition of HRTEM images and videos, nanobeam electron diffraction, and EELS were performed under this reducing condition. *In situ* HRTEM imaging of the oxide reduction process was performed with 0.5 s per frame. EELS analysis was used to determine the oxidation state of the reduced oxide. Following background removal, the spectra were deconvoluted, and two arctangent functions were then applied[56] to remove the postedge background to produce isolated Fe L_3 and L_2 edges for the calculation of the L_3/L_2 ratio (white line ratio),[56] which is proportional to the oxidation state of Fe. To minimize the effect of electron beam induced oxide reduction, the e-beam was blanked except for data acquisition. We also examined the possible effect of electron beam irradiation by comparing the oxide reduction with and without electron beam and different sample areas. Our results indicate the negligible effect of electron irradiation on the observed oxide reduction pathway.

ASSOCIATED CONTENT

Supporting Information

The Supporting Information is available free of charge on the ACS Publications website at DOI: 10.1021/acsnano.6b06950.

Detailed procedure to distinguish between γ-Fe_2O_3 and Fe_3O_4 *via* EELS measurements of the oxidation state of Fe in the oxides (PDF)

Video 1: *In situ* HRTEM visualization of the transformation from γ-Fe_2O_3 to γ-Fe_2O_3-superstructure (AVI)

Video 2: Time sequence of HRTEM images of the transformation from Fe_3O_4 to FeO (AVI)

Video 3: Output video generated by real time analysis of the atomic resolution video (Video 2): triangles show the atomic positions and the nearest neighbor distances representing Fe_3O_4 structure that decrease with time as it converts to FeO structure (the measured rate is plotted in Figure 6(g)) (AVI)

AUTHOR INFORMATION

Corresponding Authors

*E-mail: renu.sharma@nist.gov.

*E-mail: gzhou@binghamton.edu.

ORCID

Guangwen Zhou: 0000-0002-9243-293X

Present Address

[‖]Naval Research Laboratory, 4555 Overlook Ave SW, Washington, DC 20375, United States

Notes

The authors declare no competing financial interest.

ACKNOWLEDGMENTS

This work was supported by the National Science Foundation under NSF CAREER Award Grant CMMI-1056611.

REFERENCES

(1) Kabelitz, A.; Guilherme, A.; Joester, M.; Reinholz, U.; Radtke, M.; Bienert, R.; Schulz, K.; Schmack, R.; Kraehnert, R.; Emmerling, F. Time-resolved *in situ* Studies on the Formation Mechanism of Iron Oxide Nanoparticles using Combined Fast-XANES and SAXS. *CrystEngComm* **2015**, *17*, 8463−8470.

(2) Lu, J.; Jung Lee, Y.; Luo, X.; Chun Lau, K.; Asadi, M.; Wang, H.-H.; Brombosz, S.; Wen, J.; Zhai, D.; Chen, Z.; Miller, D. J.; Sub Jeong, Y.; Park, J.-B.; Zak Fang, Z.; Kumar, B.; Salehi-Khojin, A.; Sun, Y.-K.; Curtiss, L. A.; Amine, K. A Lithium−oxygen Battery Based on Lithium Superoxide. *Nature* **2016**, *529*, 377−382.

(3) Giordano, L.; Cinquini, F.; Pacchioni, G. Tuning the Surface Metal Work Function by Deposition of Ultrathin Oxide Films: Density Functional Calculations. *Phys. Rev. B: Condens. Matter Mater. Phys.* **2006**, *73*, 045414.

(4) Wang, Z. L. Functional Oxide Nanobelts: Materials, Properties and Potential Applications in Nanosystems and Biotechnology. *Annu. Rev. Phys. Chem.* **2004**, *55*, 159−196.

(5) Chen, P.; Mitsui, T.; Farmer, D. B.; Golovchenko, J.; Gordon, R. G.; Branton, D. Atomic layer deposition to fine-tune the surface properties and diameters of fabricated nanopores. *Nano Lett.* **2004**, *4*, 1333−1337.

(6) Sundman, B. An Sssessment of the Fe-O System. *J. Phase Equilib.* **1991**, *12*, 127−140.

(7) Pham, A. L.-T.; Lee, C.; Doyle, F. M.; Sedlak, D. L. A Silica-Supported Iron Oxide Catalyst Capable of Activating Hydrogen Peroxide at Neutral PH Values. *Environ. Sci. Technol.* **2009**, *43*, 8930−8935.

DOI: 10.1021/acsnano.6b06950
ACS Nano 2017, 11, 656−664

(8) Mema, R.; Yuan, L.; Du, Q.; Wang, Y.; Zhou, G. Effect of Surface Stresses on CuO Nanowire Growth in the Thermal Oxidation of Copper. *Chem. Phys. Lett.* **2011**, *512*, 87−91.
(9) Feng, H.; Wang, Y.; Wang, C.; Diao, F.; Zhu, W.; Mu, P.; Yuan, L.; Zhou, G.; Rosei, F. Defect-induced Enhanced Photocatalytic Activities of Reduced α-Fe_2O_3 Nanoblades. *Nanotechnology* **2016**, *27*, 295703.
(10) Charvin, P.; Abanades, S.; Flamant, G.; Lemort, F. Two-step water splitting thermochemical cycle based on iron oxide redox pair for solar hydrogen production. *Energy* **2007**, *32*, 1124−1133.
(11) Tilley, S. D.; Cornuz, M.; Sivula, K.; Grätzel, M. Light-Induced Water Splitting with Hematite: Improved Nanostructure and Iridium Oxide Catalysis. *Angew. Chem.* **2010**, *122*, 6549−6552.
(12) Cesar, I.; Kay, A.; Gonzalez Martinez, J. A.; Grätzel, M. Translucent thin film Fe_2O_3 photoanodes for efficient water splitting by sunlight: nanostructure-directing effect of Si-doping. *J. Am. Chem. Soc.* **2006**, *128*, 4582−4583.
(13) Arshak, K.; Gaidan, I. Development of a novel gas sensor based on oxide thick films. *Mater. Sci. Eng., B* **2005**, *118*, 44−49.
(14) Tandon, R.; Tripathy, M.; Arora, A.; Hotchandani, S. Gas and Humidity Response of Iron Oxide—Polypyrrole Nanocomposites. *Sens. Actuators, B* **2006**, *114*, 768−773.
(15) Yang, X.; Hong, H.; Grailer, J. J.; Rowland, I. J.; Javadi, A.; Hurley, S. A.; Xiao, Y.; Yang, Y.; Zhang, Y.; Nickles, R. J. cRGD-functionalized, DOX-conjugated, and 64 Cu-labeled Superparamagnetic Iron Oxide Nanoparticles for Targeted Anticancer Drug Delivery and PET/MR Imaging. *Biomaterials* **2011**, *32*, 4151−4160.
(16) Chertok, B.; Moffat, B. A.; David, A. E.; Yu, F.; Bergemann, C.; Ross, B. D.; Yang, V. C. Iron oxide nanoparticles as a drug delivery vehicle for MRI monitored magnetic targeting of brain tumors. *Biomaterials* **2008**, *29*, 487−496.
(17) He, K.; Xu, C.-Y.; Zhen, L.; Shao, W.-Z. Hydrothermal Synthesis and Characterization of Single-crystalline Fe_3O_4 Nanowires with High Aspect Ratio and Uniformity. *Mater. Lett.* **2007**, *61*, 3159−3162.
(18) He, K.; Xu, C.-Y.; Zhen, L.; Shao, W.-Z. Fractal Growth of Single-crystal α-Fe_2O_3: from Dendritic Micro-pines to Hexagonal Micro-snowflakes. *Mater. Lett.* **2008**, *62*, 739−742.
(19) He, K.; Zhang, S.; Li, J.; Yu, X.; Meng, Q.; Zhu, Y.; Hu, E.; Sun, K.; Yun, H.; Yang, X.-Q.; Zhu, Y.; Gan, H.; Mo, Y.; Stach, E. A.; Murray, C. B.; Su, D. Visualizing Non-equilibrium Lithiation of Spinel Oxide *via in situ* Transmission Electron Microscopy. *Nat. Commun.* **2016**, *7*, 11441.
(20) Yuan, L.; Wang, Y.; Cai, R.; Jiang, Q.; Wang, J.; Li, B.; Sharma, A.; Zhou, G. The Origin of Hematite Nanowire Growth during the Thermal Oxidation of Iron. *Mater. Sci. Eng., B* **2012**, *177*, 327−336.
(21) Cao, X.; Wang, N. A novel non-enzymatic glucose sensor modified with Fe_2O_3 nanowire arrays. *Analyst* **2011**, *136*, 4241−4246.
(22) Mohapatra, S. K.; John, S. E.; Banerjee, S.; Misra, M. Water Photooxidation by Smooth and Ultrathin α-Fe_2O_3 Nanotube Arrays. *Chem. Mater.* **2009**, *21*, 3048−3055.
(23) Zhu, W.; Winterstein, J. P.; Sharma, R.; Zhou, G. Atomic-Scale Characterization of the Reduction of a-Fe_2O_3 Nanowires. *Microsc. Microanal.* **2015**, *21*, 995−996.
(24) Yuan, L.; Cai, R.; Jang, J. I.; Zhu, W.; Wang, C.; Wang, Y.; Zhou, G. Morphological transformation of hematite nanostructures during oxidation of iron. *Nanoscale* **2013**, *5*, 7581−7588.
(25) Yang, P.; Ding, Y.; Lin, Z.; Chen, Z.; Li, Y.; Qiang, P.; Ebrahimi, M.; Mai, W.; Wong, C. P.; Wang, Z. L. Low-cost High-performance Solid-state Asymmetric Supercapacitors Based on MnO_2 Nanowires and Fe_2O_3 Nanotubes. *Nano Lett.* **2014**, *14*, 731−736.
(26) Hou, Y.; Zuo, F.; Dagg, A.; Feng, P. Visible Light-Driven α-Fe_2O_3 Nanorod/Graphene/$BiV_{1-x}Mo_xO_4$ Core/Shell Heterojunction Array for Efficient Photoelectrochemical Water Splitting. *Nano Lett.* **2012**, *12*, 6464−6473.
(27) Yuan, L.; Wang, Y.; Mema, R.; Zhou, G. Driving Force and Growth Mechanism for Spontaneous Oxide Nanowire Formation during the Thermal Oxidation of Metals. *Acta Mater.* **2011**, *59*, 2491−2500.
(28) Cai, R.; Li, T.; Wang, Y.; Wang, C.; Yuan, L.; Zhou, G. Formation of modulated structures in single-crystalline hexagonal α-Fe_2O_3 nanowires. *J. Nanopart. Res.* **2012**, *14*, 1073.
(29) Fu, Y.; Wang, R.; Xu, J.; Chen, J.; Yan, Y.; Narlikar, A.; Zhang, H. Synthesis of Large Arrays of Aligned α-Fe_2O_3 Nanowires. *Chem. Phys. Lett.* **2003**, *379*, 373−379.
(30) Cvelbar, U.; Chen, Z.; Sunkara, M. K.; Mozetič, M. Spontaneous Growth of Superstructure α-Fe_2O_3 Nanowire and Nanobelt Arrays in Reactive Oxygen Plasma. *Small* **2008**, *4*, 1610−1614.
(31) Morales, A. M.; Lieber, C. M. A Laser Ablation Method for the Synthesis of Crystalline Semiconductor Nanowires. *Science* **1998**, *279*, 208−211.
(32) Zhu, W.; Winterstein, J.; Maimon, I.; Yin, Q.; Yuan, L.; Kolmogorov, A. N.; Sharma, R.; Zhou, G. Atomic Structural Evolution during the Reduction of α-Fe_2O_3 Nanowires. *J. Phys. Chem. C* **2016**, *120*, 14854−14862.
(33) Zhu, W.; Winterstein, J. P.; Sharma, R.; Zhou, G. *In situ* Atomic-Scale Visualization of CuO Nanowire Growth. *Microsc. Microanal.* **2016**, *22*, 1588−1589.
(34) Zhu, W.; Winterstein, J. P.; Sharma, R.; Zhou, G. The Growth of Catalyst-free NiO Nanowires. *Microsc. Microanal.* **2016**, *22*, 1620−1621.
(35) Yuan, L.; Jiang, Q.; Wang, J.; Zhou, G. The Growth of Hematite Nanobelts and Nanowires — Tune the Shape *via* Oxygen Gas Pressure. *J. Mater. Res.* **2012**, *27*, 1014−1021.
(36) Wang, Y.; Wang, C.; Yuan, L.; Cai, R.; Liu, X.; Li, C.; Zhou, G. Coincidence-Site-Lattice Twist Boundaries in Bicrystalline α-Fe_2O_3 Nanoblades. *J. Phys. Chem. C* **2014**, *118*, 5796−5801.
(37) Glezer, A.; Stolyarov, V.; Tomchuk, A.; Shurygina, N. Grain Boundary Engineering and Superstrength of Nanocrystals. *Tech. Phys. Lett.* **2016**, *42*, 51−54.
(38) Bollmann, W. *Crystal defects and crystalline interfaces*; Springer Science & Business Media: New York, 2012.
(39) Yuan, L.; Van Der Geest, A. G.; Zhu, W.; Yin, Q.; Li, L.; Kolmogorov, A. N.; Zhou, G. Reduction of CuO Nanowires Confined by a Nano Test Tube. *RSC Adv.* **2014**, *4*, 30259−30266.
(40) Yang, Y.; Luo, L.-M.; Guo, Y.-F.; Dai, Z.-X.; Zhang, R.-H.; Sun, C.; Zhou, X.-W. *In situ* Synthesis of PtPd Pimetallic Nanocatalysts Supported on Graphene Nanosheets for Methanol Oxidation Using Triblock Copolymer as Reducer and Stabilizer. *J. Electroanal. Chem.* **2016**, *783*, 132.
(41) Andersson, A.; Holmberg, J.; Häggblad, R. Process Improvements in Methanol Oxidation to Formaldehyde: Application and Catalyst Development. *Top. Catal.* **2016**, *59*, 1589−1599.
(42) Watanabe, R.; Watanabe, S.; Hirata, N.; Fukuhara, C. Effect of Promoter Addition on Water Gas Shift Property over Structured-Type Iron Oxide Catalyst. *Catal. Lett.* **2016**, *146*, 2478−2484.
(43) Dong, Z.; Wang, T.; Zhao, J.; Fu, T.; Wang, L.; Li, J.; Ding, W. Catalytic Performance of Iron Oxide Loaded on Electron-rich Surfaces of Carbon Nitride. *J. Energy Chem.* **2016**, *25*, 1021.
(44) Lang, C.; Sécordel, X.; Kiennemann, A.; Courson, C. Water Gas Shift Catalysts for Hydrogen Production from Biomass Steam Gasification. *Fuel Process. Technol.* **2017**, *156*, 246.
(45) Kachi, S.; Momiyama, K.; Shimizu, S. An Electron Diffraction Study and a Theory of the Transformation from g-Fe_2O_3 to a-Fe_2O_3. *J. Phys. Soc. Jpn.* **1963**, *18*, 106−116.
(46) Chen, Z.; Cvelbar, U.; Mozetič, M.; He, J.; Sunkara, M. K. Long-Range Ordering of Oxygen-Vacancy Planes in α-Fe_2O_3 Nanowires and Nanobelts. *Chem. Mater.* **2008**, *20*, 3224−3228.
(47) Koga, Y.; Harrison, L. *Comprehensive Chemical Kinetics*; Bamford, C. H., Tipper, C. F. H., Compton, R. G., Eds.; Elsevier: Amsterdam, The Netherlands, 1984; Vol. *21*, p 120
(48) Rodriguez, J. A.; Hanson, J. C.; Frenkel, A. I.; Kim, J. Y.; Pérez, M. Experimental and Theoretical Studies on the Reaction of H_2 with NiO: Role of O Vacancies and Mechanism for Oxide Reduction. *J. Am. Chem. Soc.* **2002**, *124*, 346−354.
(49) Kim, J. Y.; Rodriguez, J. A.; Hanson, J. C.; Frenkel, A. I.; Lee, P. L. Reduction of CuO and Cu_2O with H_2: H Embedding and Kinetic

DOI: 10.1021/acsnano.6b06950
ACS Nano 2017, 11, 656−664

Effects in the Formation of Suboxides. *J. Am. Chem. Soc.* **2003**, *125*, 10684−10692.
(50) Zhou, G.; Yang, J. C. Reduction of Cu_2O Islands Grown on a Cu(100) Surface through Vacuum Annealing. *Phys. Rev. Lett.* **2004**, *93*, 226101.
(51) Wang, C. M.; Baer, D. R.; Thomas, L. E.; Amonette, J. E.; Antony, J.; Qiang, Y.; Duscher, G. Void Formation during Early Stages of Passivation: Initial Oxidation of Iron Nanoparticles at Room Temperature. *J. Appl. Phys.* **2005**, *98*, 094308.
(52) Sharma, G.; Jeevanandam, P. Synthesis of Self-assembled Prismatic Iron Oxide Nanoparticles by a Novel Thermal Decomposition Route. *RSC Adv.* **2013**, *3*, 189−200.
(53) Jozwiak, W.; Kaczmarek, E.; Maniecki, T.; Ignaczak, W.; Maniukiewicz, W. Reduction Behavior of Iron Oxides in Hydrogen and Carbon Monoxide Atmospheres. *Appl. Catal., A* **2007**, *326*, 17−27.
(54) Yuan, L.; Jiang, Q.; Wang, J.; Zhou, G. The growth of hematite nanobelts and nanowires—tune the shape via oxygen gas pressure. *J. Mater. Res.* **2012**, *27*, 1014−1021.
(55) Sharma, R. An Environmental Transmission Electron Microscope for *in situ* Synthesis and Characterization of Nanomaterials. *J. Mater. Res.* **2005**, *20*, 1695−1707.
(56) Cave, L.; Al, T.; Loomer, D.; Cogswell, S.; Weaver, L. A STEM/EELS method for mapping iron valence ratios in oxide minerals. *Micron* **2006**, *37*, 301−309.

DOI: 10.1021/acsnano.6b06950
ACS Nano 2017, 11, 656−664